THE ASTROPHYSICAL JOURNAL, 1001:161 (15pp), 2026 April 20 https://doi.org/10.3847/1538-4357/ae5224

The ALMA-QUARKS Survey: Evidence of an Explosive Molecular Outflow in IRAS 15520–5234

Ariful Hoque[1], Tapas Baug[1], Estrella Guzman[2], Manuel Fernandez Lopez[2], Tie Liu[3,4], Guido Garay[5,6], Paul F. Goldsmith[7], Fengwei Xu[8], Xindi Tang[9], Patricio Sanhueza[10], Lokesh K. Dewangan[11], Shivani Gupta[12,13], Sami Dib[8], Luis A. Zapata[14], Jihye Hwang[15,16], N. K. Bhadari[17], John Bally[18], Swagat Ranjan Das[5], Aiyuan Yang[19,20], Prasanta Gorai[21,22], Arup Kumar Maity[11], James O. Chibueze[23,24,25], Pablo García[6,26], Leonardo Bronfman[5], Xunchuan Liu[3], L. Viktor Tóth[27], Shehu Muhammad Usman[1], and Kee-Tae Kim[28,29]

[1] S. N. Bose National Centre for Basic Sciences, Block-JD, Sector-III, Salt Lake City, Kolkata 700106, India; arifulh882@gmail.com
[2] Instituto Argentino de Radioastronomía (CCT-La Plata, CONICET, UNLP, CICPBA), C.C. No. 5, 1894, Villa Elisa, Buenos Aires, Argentina
[3] Shanghai Astronomical Observatory, Chinese Academy of Sciences, 80 Nandan Road, Shanghai 200030, People's Republic of China
[4] Key Laboratory for Research in Galaxies and Cosmology, Shanghai Astronomical Observatory, Chinese Academy of Sciences, 80 Nandan Road, Shanghai 200030, People's Republic of China
[5] Departamento de Astronomía, Universidad de Chile, Las Condes, Santiago 7550000, Chile
[6] Chinese Academy of Sciences South America Center for Astronomy, National Astronomical Observatories, CAS, Beijing 100101, People's Republic of China
[7] Jet Propulsion Laboratory, California Institute of Technology, 4800 Oak Grove Drive, Pasadena, CA 91109, USA
[8] Max Planck Institute for Astronomy, Königstuhl 17, 69117 Heidelberg, Germany
[9] XingJiang Astronomical Observatory, Chinese Academy of Sciences (CAS), Urumqi 830011, People's Republic of China
[10] Department of Astronomy, School of Science, The University of Tokyo, 7-3-1 Hongo, Bunkyo, Tokyo 113-0033, Japan
[11] Physical Research Laboratory, Navrangpura, Ahmedabad 380009, India
[12] Indian Institute of Astrophysics, II Block, Koramangala, Bengaluru 560034, India
[13] Pondicherry University, R.V. Nagar, Kalapet, 605014, Puducherry, India
[14] Instituto de Radioastronomía y Astrofísica, Universidad Nacional Autónoma de México, 58090, Morelia, Michoacán, Mexico
[15] Institute for Advanced Study, Kyushu University, Japan
[16] Department of Earth and Planetary Sciences, Faculty of Science, Kyushu University, Nishi-ku, Fukuoka 819-0395, Japan
[17] Kavli Institute for Astronomy and Astrophysics, Peking University, 5 Yiheyuan Road, Haidian District, Beijing 100871, People's Republic of China
[18] CASA, University of Colorado, 389-UCB, Boulder, CO 80309, USA
[19] National Astronomical Observatories, Chinese Academy of Sciences, Beijing 100101, People's Republic of China
[20] Key Laboratory of Radio Astronomy and Technology, Chinese Academy of Sciences, A20 Datun Road, Chaoyang District, Beijing, 100101, People's Republic of China
[21] Rosseland Centre for Solar Physics, University of Oslo, P.O. Box 1029 Blindern, 0315 Oslo, Norway
[22] Institute of Theoretical Astrophysics, University of Oslo, P.O. Box 1029 Blindern, 0315 Oslo, Norway
[23] UNISA Centre for Astrophysics and Space Sciences (UCASS), College of Science, Engineering and Technology, University of South Africa, Cnr Christian de Wet Rd and Pioneer Avenue, Florida Park, 1709, Roodepoort, South Africa
[24] Centre for Space Research, North-West University, Potchefstroom 2520, South Africa
[25] Department of Physics and Astronomy, Faculty of Physical Sciences, University of Nigeria, Carver Building, 1 University Road, Nsukka 410001, Nigeria
[26] Instituto de Astronomía, Universidad Católica del Norte, Av. Angamos 0610, Antofagasta, Chile
[27] University of Debrecen, Institute of Physics, H-4032 Debrecen, Bem tér 1, Hungary
[28] Korea Astronomy and Space Science Institute, 776 Daedeokdae-ro, Yuseong-gu, Daejon 34055, Republic of Korea
[29] University of Science and Technology, Korea (UST), 217 Gajeong-ro, Yuseong-gu, Daejeon, 34113, Republic of Korea

Received 2025 November 28; revised 2026 March 10; accepted 2026 March 13; published 2026 April 14

Abstract

We present a study of the massive protocluster IRAS 15520–5234, which displays evidence of an explosive molecular outflow that unleashed a kinetic energy of at least 10^{48} erg. The protocluster contains 16 dense cores detected in the Atacama Large Millimeter/submillimeter Array (ALMA) band 6 continuum emission maps, having masses in the range from 0.2 to 11.0 $M_{\odot}$. Our analysis of CO (2−1) emission reveals 28 well-collimated outflow fingers, the majority of which follow a Hubble–Lemaître velocity law. The outflow fingers show no preferred orientation in the plane of sky and emerge from a common center of origin. We estimate the total mass, momentum, and kinetic energy of the outflow fingers and find that the values are at least 1 order of magnitude higher than the typical bipolar outflows associated with massive protostars. The morphology and kinematics of the outflow fingers suggest that the outflow associated with IRAS 15520–5234 is explosive in nature. We calculate the dynamical age of the explosive event to be approximately 6550 yr. Additionally, we estimate the frequency of such explosive outflows in the Galaxy, which is one event every 83 yr. Finally, we speculate that the rearrangement of masses within the massive protocluster and the dynamical interaction among the massive cores may result in the formation of such an energetic event.

Unified Astronomy Thesaurus concepts: Star forming regions (1565); Interstellar medium (847); Submillimeter astronomy (1647); Protostars (1302); Interstellar molecules (849)

1. Introduction

Massive protoclusters are the birthplaces of most of the massive stars and play a crucial role in their formation and evolution within molecular clouds. These massive protoclusters are often associated with highly energetic outflows that act

Table 1
Summary of the Spectral Lines from the ALMA-QUARKS Survey Analyzed in This Study

Molecule	Transition	Rest Frequency (GHz)	Synthesized Beam Size (arcsec × arcsec)	Spectral Resolution (km s^{-1})	rms per 0.488 MHz Channel (mJy $beam^{-1}$)
SiO	5−4	217.104919	0.41×0.36	1.35	6.2
CH_3OH	4(2, 2) −3(1, 2)	218.440063	0.41×0.36	1.34	5.8
SO	6(5)−5(4)	219.949442	0.42×0.40	1.33	6.7
^{13}CO	2−1	220.398684	0.42×0.39	1.32	7.8
^{12}CO	2−1	230.538000	0.40×0.37	1.27	8.2
$H_{30\alpha}$	⋯	231.900928	0.40×0.37	1.26	6.0

as a primary mechanism for the release of gravitational potential energy. During the initial phases of protostellar evolution, two types of molecular outflows are observed—the classical bipolar outflows and explosive outflows. Bipolar outflows are generated through active accretion onto the central protostar via a flattened disk. These types of outflows are observed in both low-mass and high-mass star-forming regions (R. Bachiller 1996; A. López-Sepulcre et al. 2009; H. G. Arce et al. 2010; L. T. Maud et al. 2015; T. Baug et al. 2020; N. Guerra-Varas et al. 2023; A. P. M. Towner et al. 2024; A. Hoque et al. 2025, and references therein). Explosive outflows are a distinct and highly energetic category of molecular outflows (L. A. Zapata et al. 2009, 2013, 2019; J. Bally et al. 2022; E. Guzmán Ccolque et al. 2022). They are characterized by multiple narrow filaments emerging out of a common center and follow a Hubble–Lemaître velocity law, i.e., linearly increasing velocity of the outflowing gas with distance from the common center. While bipolar outflows are studied extensively in both low- and high-mass star formation, the study of explosive outflows is limited due to their rarity and shorter timescales. To date, only seven explosive outflow events have been reported in our Galaxy, and all of them are associated with massive star-forming regions (L. A. Zapata et al. 2009, 2013, 2019; J. Bally et al. 2022; E. Guzmán Ccolque et al. 2022; L. A. Zapata et al. 2023; N. Issac et al. 2025).

Multiple theoretical and analytical models have been proposed and tested to explain the origin of explosive outflows (J. Bally et al. 2011; A. C. Raga et al. 2021; P. R. Rivera-Ortiz et al. 2021, 2025). For example, J. Bally et al. (2011) proposed that the rearrangement of nonhierarchical systems and their dynamical interactions can lead to the formation of explosive outflows. P. R. Rivera-Ortiz et al. (2021) performed an *N*-body simulation that accounts for the close encounter of a massive runaway star (of mass 10 $M_\odot$) with a cluster of massive particles and found that when the mass of the cluster is less than or up to a few times of the stellar mass, the collision between them will produce an explosive outflow.

The massive protocluster IRAS 15520–5234 (hereafter I15520) is located at a distance of 2.56 kpc and has a local standard of rest velocity $V_{\rm lsr}$ of −41.8 km s^{-1} (X. Liu et al. 2024). The associated massive clump has mass and luminosity of $10^{3.2}$ $M_\odot$ and $10^{5.1}$ $L_\odot$, respectively (J. S. Urquhart et al. 2017; T. Liu et al. 2020). The protocluster is also associated with evolved ultracompact (UC) H II regions (S. P. Ellingsen et al. 2005). Molecular outflows have been identified with the Atacama Large Millimeter/submillimeter Array (ALMA) band 7 at 0.87 mm by T. Baug et al. (2020) in the region. The authors have identified a total of seven outflow lobes (five blueshifted and two redshifted) associated with 0.87 mm continuum cores. In another study by F. Xu et al. (2023), multiple prestellar and protostellar cores were identified in the region with ALMA band 7. Our recent ALMA-ATOMS survey of HC_3N outflows has revealed the presence of multiple outflow lobes (four blueshifted and three redshifted) emerging out of a single core (at an angular resolution of ∼1$''$.7), hinting to an explosive outflow event in I15520 (A. Hoque et al. 2025).

In this study, we utilized high-resolution ALMA band 6 data from the Querying Underlying Mechanisms of Massive Star Formation with ALMA-Resolved Gas Kinematics and Structures (QUARKS) survey and detected 28 outflow fingers associated with I15520. We confirm the explosive nature of the outflow fingers and investigate the possible driving mechanism of the explosive event. The paper is organized in the following manner. In Section 2, we introduce the ALMA data and other archival data used in this study. Section 3 presents the identification of continuum cores, outflow fingers, the study of outflow morphology and kinematics, and the radio emissions associated with the explosive outflow. In Section 4, we present a discussion about the explosive nature of the outflow associated with I15520, the frequency of occurrence of such energetic events in our Galaxy, and the possible driving mechanism of the explosive event. Finally, a summary of this work is presented in Section 5.

2. Observations and Data

2.1. ALMA Observations

In this study, we utilize ALMA band 6 data from the QUARKS (X. Liu et al. 2024) survey. The QUARKS survey includes 139 massive star-forming regions, observed using both the ALMA 12 m compact array and Atacama Compact Array (ACA) 7 m array in ALMA band 6. More comprehensive details of the observations and data reductions can be found in X. Liu et al. (2024). In our study, we use the 12 m array + ACA 7 m array combined data, which has a beam size of ∼0$''$.36 × 0$''$.33 and an rms noise level of 0.2 mJy $beam^{-1}$. The details of the molecular line data from the QUARKS survey used in this study are mentioned in Table 1.

2.2. Archival Data

The Spitzer Space Telescope Infrared Array Camera (IRAC) Ch1 (3.6 μm) and Ch2 (4.5 μm) archival images were obtained from the Galactic Legacy Infrared Midplane Survey Extraordinaire (GLIMPSE; R. A. Benjamin et al. 2003) survey. The Spitzer-IRAC images have a spatial resolution of ∼2$''$.0 and a sensitivity of ∼0.2–0.3 mJy $beam^{-1}$.

We utilize the 5.5 GHz radio continuum image from the Coordinated Radio "N" Infrared Survey for High-mass Star Formation (CORNISH-SOUTH; T. Irabor et al. 2023) survey

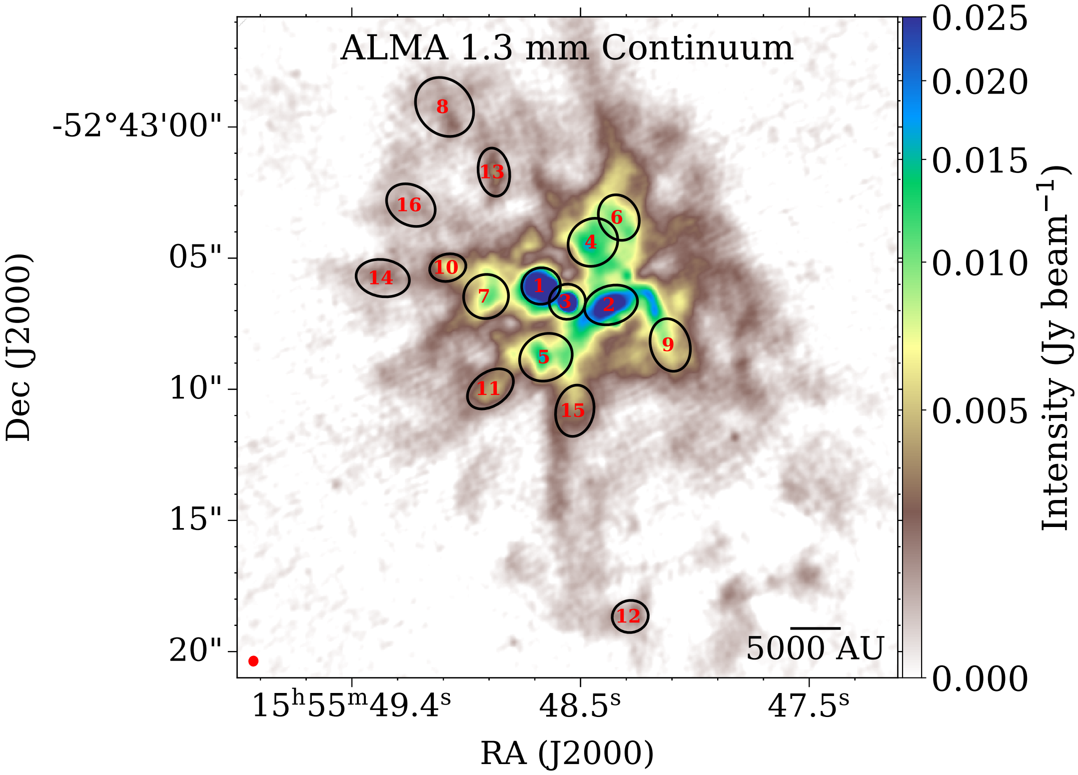

Figure 1. ALMA 1.3 mm continuum emission in the region I15520. The black ellipses represent the cores identified by D. Yang et al. (2025) using the *getsf* algorithm. The cores are labeled numerically (in red) in the order they were identified in *getsf*. The beam is shown in the bottom-left corner, and the scale bar is shown in the bottom-right corner.

to identify the ionized emissions in the region. The CORNISH-SOUTH image has an angular resolution of ∼2.″5 and an rms noise of ∼0.11 mJy beam^{-1}.

3. Results

3.1. 1.3 mm Continuum Emission

In Figure 1, we present the 1.3 mm continuum emission maps for I15520, overlaid with the compact cores identified previously in the ALMA-QUARKS survey (QUARKS-III; D. Yang et al. 2025). In D. Yang et al. (2025), the *getsf* source extraction algorithm (A. Men'shchikov 2021) was adopted to extract the cores from the high-resolution ALMA 1.3 mm continuum map. Using molecular line data, the cores were further classified into different evolutionary stages, starting from starless cores to UC H II regions. A total of 16 compact cores were identified in the region. Among them, 10 were classified as hot molecular cores (HMCs), and the remaining 6 were classified as UC H II regions. The authors estimated the masses of the cores, assuming a dust temperature of 100 K for the evolved cores (see D. Yang et al. 2025 for details). Note that the 1.3 mm continuum map might be affected by free–free emissions and this could lead to the overestimation of the masses of the continuum cores. Table 2 lists the details of the continuum cores associated with I15520.

3.2. Identification of Outflows and Their Kinematics

We utilize the ^{12}CO ($J = 2-1$) (hereafter CO) molecular line data from the ALMA band 6 observations for the identification and kinematic study of the outflow fingers. We generate the integrated intensity (i.e., moment 0) and the intensity-weighted velocity (i.e., moment 1) maps using the `spectral-cube` package from the `astropy` project (Astropy Collaboration et al. 2013). The top-left panel of Figure 2 shows the CO moment 0 map, tracing the isotropic distribution of fingerlike outflow structures, while the top-right panel presents the CO moment 1 map, tracing the velocity of these structures. The bottom panel of Figure 2 shows the normalized spectra of the CO emissions marked with regions of blue- and redshifted wing emissions in blue and red hatches. The CO emissions show self-absorption toward the central velocity of the cloud. Therefore, to exclude the contamination of the central cloud and mitigate the effect of self-absorption, we exclude the velocity range −50.0 to −36.0 km s^{-1} for the estimation of outflow parameters and kinematics. We generate the blue- and redshifted outflow wing emission maps by integrating emission in the velocity ranges [−76.0, −50.0] and [−36.0, −12.0] km s^{-1}, respectively. We present the blue-shifted and redshifted wing emission maps in Figure 3.

We further investigate the CO data by generating channel maps for the blue- and redshifted outflow components in the velocity range [−76.0, −50.0] and [−36.0, −12.0] km s^{-1}, respectively, with each channel representing integrated intensity within 2 km s^{-1} velocity width. The CO channel maps are presented in the Appendix A (see Figures A1 and A2). The outflow fingers in Figures A1 and A2 appear to be randomly oriented in the plane of sky. Outflow fingers are identified by investigating consecutive velocity channels, starting from the outermost velocity channels in the blue- and redshifted directions with respect to the V_{lsr}. We generate contour at emissions ⩾5σ (where σ represents the rms of the background noise) in each velocity channel and trace the "spines" along the emission peaks. Finally, by aggregating the

Table 2
Parameters of the 1.3 mm Continuum Cores (D. Yang et al. 2025)

Core No.	R.A. (J2000) (hh:mm:ss)	Decl. (J2000) (dd:mm:ss)	FWHM$_{\rm maj}$ (arcsec)	FWHM$_{\rm min}$ (arcsec)	PA[a] (deg)	F$^{\dagger}_{\rm int}$ [a] (mJy)	Core Mass[b] ($M_\odot$)	Evolutionary Stage
1	15:55:48.65	−52:43:06.10	1.482	1.388	100.3	362.2(3.9)	8.16(3.29)	UC H II
2	15:55:48.36	−52:43:06.82	2.061	1.459	106.3	484.3(7.4)	10.95(4.43)	UC H II
3	15:55:48.54	−52:43:06.70	1.387	1.338	14.2	220.4(3.9)	4.95(2.05)	UC H II
4	15:55:48.44	−52:43:04.44	1.953	1.769	34.7	153.8(5.8)	3.48(1.46)	HMC
5	15:55:48.63	−52:43:08.82	2.055	1.766	115.0	98.6(5.5)	2.24(0.92)	UC H II
6	15:55:48.33	−52:43:03.49	1.791	1.500	26.8	60.3(3.9)	1.37(0.56)	HMC
7	15:55:48.89	−52:43:06.50	1.724	1.670	118.1	81.6(4.0)	1.84(0.78)	HMC
8	15:55:49.06	−52:42:59.27	2.422	2.026	42.6	36.2(2.2)	0.82(0.35)	HMC
9	15:55:48.11	−52:43:08.35	2.037	1.495	15.3	39.5(4.3)	0.89(0.38)	UC H II
10	15:55:49.05	−52:43:05.40	1.397	1.034	102.7	20.9(3.0)	0.47(0.20)	HMC
11	15:55:48.87	−52:43:10.02	1.944	1.277	125.0	21.4(2.6)	0.48(0.21)	HMC
12	15:55:48.28	−52:43:18.70	1.379	1.221	99.6	10.5(0.7)	0.24(0.10)	HMC
13	15:55:48.85	−52:43:01.76	1.847	1.189	8.8	11.1(1.3)	0.25(0.11)	HMC
14	15:55:49.32	−52:43:05.80	2.045	1.409	81.2	15.2(1.6)	0.34(0.14)	HMC
15	15:55:48.51	−52:43:10.86	1.972	1.445	168.6	9.5(2.0)	0.21(0.10)	UC H II
16	15:55:49.20	−52:43:03.02	1.957	1.502	60.4	9.2(1.7)	0.21(0.09)	HMC

Notes.

[a] PA: Position angle of the core major axis, measured East of North.

[b] The measurement uncertainty is shown in the parentheses.

spines from all velocity channels, we map the trajectories of the outflow fingers. We find a total of 14 blueshifted and 14 redshifted narrow outflow fingers emerging from the central cloud. Although the outflow fingers are believed to originate from a common center, pinpointing the exact location is challenging, as some fingers show no emissions toward the cloud center. Therefore, we define a common center of origin at R.A.: $15^{\rm h}55^{\rm m}48\overset{\rm s}{.}51$, decl.:$-52^{\rm d}43^{\rm m}07\overset{\rm s}{.}11$, with a box of size $4\overset{\prime\prime}{.}5 \times 4\overset{\prime\prime}{.}5$ such that, when extended in the backward direction, the outflow fingers approximately converge within this box. In Figure 3, we mark the blue- and redshifted outflow fingers with cyan and red lines and the location of the common center by a black dashed rectangle. We also search for the possibility of any bipolar outflows in the region by investigating the velocity opposite channels with respect to $V_{\rm lsr}$ ($= -41.8$ km s^{-1}) in Figures A1 and A2 and do not find any bipolar components associated with the outflow fingers.

We estimate the radial velocity of the outflow fingers from the farthest velocity channel having emissions $>5\sigma$ within the outflow fingers, where σ is the rms of the background noise, estimated from emission-free regions. Figure 4 shows the radial velocity of the outflowing gas as a function of the sky-projected distance. The blue and red lines in Figure 4 represent the radial velocity of the outflowing gas of the blue- and redshifted fingers with distance from the common center. We find a linearly increasing trend of the radial velocity of the outflowing gas with distance (Hubble–Lemaître velocity law). The linearly increasing velocity of outflowing materials are believed to be originated due to ballistic or accelerated motion of the outflowing material, driven by momentum-conserving winds (F. H. Shu et al. 1991; Z.-Y. Li & F. H. Shu 1996; H. G. Arce & A. A. Goodman 2001). Since the outflow fingers are oriented isotropically in space, the effect of different inclination angles will be added in the Hubble–Lemaître velocity law of each outflow finger. As a result, the position–velocity (P–V) diagrams of the outflow fingers will appear to have different slopes as seen in Figure 4.

Note that such kinematics of the outflow fingers, i.e., linearly increasing velocity from a common center, having different slopes of the P–V diagrams of different outflow fingers were earlier reported in explosive outflows (L. A. Zapata et al. 2009, 2013, 2019; J. Bally et al. 2022; E. Guzmán Ccolque et al. 2022; L. A. Zapata et al. 2023; E. Guzmán Ccolque et al. 2024) and are one of the most defining characteristics of this category of outflows.

3.3. *Outflow Energetics*

In this section, we estimate the physical parameters of the outflow, such as its mass, momentum, and energy. We first estimate the CO column density ($N_{\rm thin}$) assuming the emission to be optically thin following the methodology devised in R. P. Garden et al. (1991) and P. Sanhueza et al. (2012) and then corrected for optical depth of CO following P. F. Goldsmith & W. D. Langer (1999) and J. G. Mangum & Y. L. Shirley (2015).

With the assumptions for the CO emission to be optically thin and also in local thermodynamic equilibrium (LTE), we derive the CO column density following the equation (adopted from R. P. Garden et al. 1991; P. Sanhueza et al. 2012),

$$N_{\rm thin} = \frac{8\pi\nu^3}{c^3}\frac{Q_{\rm rot}}{g_{\rm u}A_{\rm ul}}\frac{\exp(E_{\rm l}/kT_{\rm ex})}{1-\exp(-h\nu/kT_{\rm ex})} \times \frac{\int T_{\rm B}dv}{J(T_{\rm B})-J(T_{\rm bg})}, \quad (1)$$

with $J(T)$ being defined as

$$J(T) = \frac{h\nu}{k}\frac{1}{e^{h\nu/kT}-1}, \quad (2)$$

where ν is the frequency of the transition, c is the speed of light, $Q_{\rm rot}$ is the partition function, $g_{\rm u}$ is the statistical weight of the upper level, $A_{\rm ul}$ is the Einstein coefficient for spontaneous emission, $E_{\rm l}$ is the energy of the lower level, $T_{\rm ex}$ is the excitation temperature, $T_{\rm B}$ is the brightness temperature, and

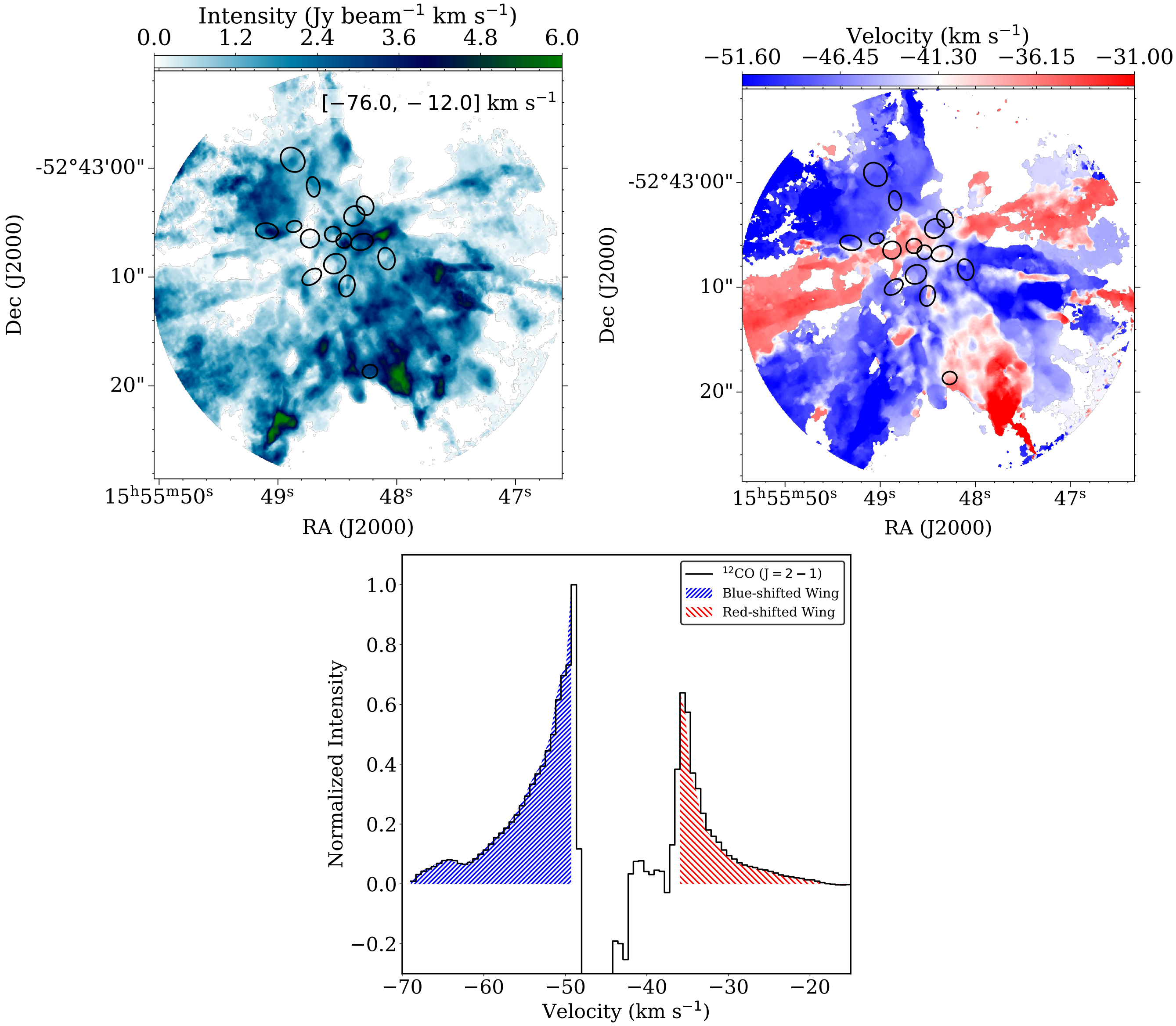

Figure 2. (Top) ALMA CO moment 0 (left) and moment 1 (right) maps of the region I15520. In each panel, the identified continuum cores are marked with black ellipses. The velocity range of integration is mentioned in the top-right corner of the CO moment 0 map. (Bottom) Normalized CO spectrum integrated over the ALMA field of view (black). The blue and red hatched regions indicate blue- and redshifted wing emissions, respectively.

$T_{\rm bg} = 2.7$ K is the cosmic microwave background temperature. In our analysis, we measure the integrated intensity over the velocity range of the outflows, which is approximately equal to $\int T_{\rm B} dv$. In Equation (2), we use a $T_{\rm ex}$ of 50 K for the outflow materials. In general, the temperature of the outflowing material lies within ∼20−100 K (J. Hatchell et al. 1999; Y. Shimajiri et al. 2009). In high-mass star-forming clumps, the gas kinetic temperature is found in the range from 30 to 200 K with an average of 62 ± 2 K (X. D. Tang et al. 2018). N. Izumi et al. (2024) also estimated the kinetic temperature of outflows for 12 massive infrared dark clouds (IRDCs) using formaldehyde (H_2CO) emissions, in the range 26 to 300 K, having an average kinetic temperature of 75 ± 50 K. The values of $Q_{\rm rot}(=kT_{\rm ex}/hB + 1/3 = 18.45)$, $g_{\rm u}(=5)$, $A_{\rm ul}(=6.911 \times 10^{-7}\ {\rm s}^{-1})$, and $E_{\rm l}(=5.53\ {\rm K})$ are obtained from the Cologne Database for Molecular Spectroscopy (CDMS; H. S. P. Müller et al. 2001) and XCLASS database (T. Möller et al. 2017).

We corrected the CO column density for not optically thin CO emission following the methodology devised in P. F. Goldsmith & W. D. Langer (1999) and J. G. Mangum & Y. L. Shirley (2015).

$$N = N_{\rm thin} \frac{\tau}{1 - \exp(-\tau)}, \tag{3}$$

where τ is the optical depth of CO.

Assuming the two isotopologues ^{12}CO (2−1) and ^{13}CO (2−1) have the same excitation temperature, we estimate τ (following K. Qiu et al. 2009) from

$$\frac{I(^{12}{\rm CO})}{I(^{13}{\rm CO})} = \frac{1 - \exp(-\tau)}{1 - \exp(-\tau/\chi)}, \tag{4}$$

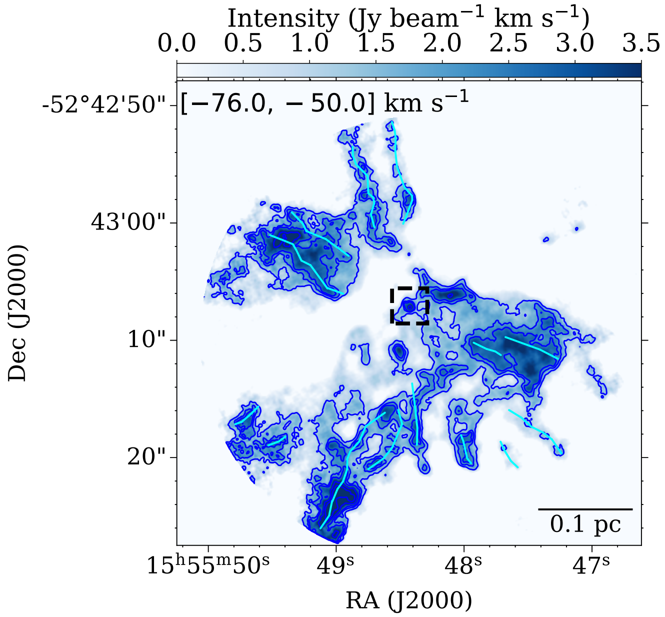

Figure 3. The CO blueshifted (left) and redshifted (right) wing emission maps. The cyan and red lines represent the blueshifted and redshifted outflow fingers, respectively. The blue (left) and red (right) contours are drawn at the levels of [5, 8, 10, 15, 20, 50]$\times\sigma$, where $\sigma = 0.15$ and 0.25 Jy beam^{-1} km s^{-1} for the blue- and redshifted wing emission maps, respectively. The velocity ranges of the wing emission maps are given in the top-left corner of each figure. The black dashed rectangle represents the region of interest from where the explosive event is possibly originating.

where χ is the abundance ratio of ^{12}CO (2−1) and ^{13}CO (2−1) derived using the relation, $\chi = (7.5 \pm 1.9)\mathrm{D_{GC}} + (7.6 \pm 12.9)$ (T. L. Wilson & R. T. Rood 1994). $\mathrm{D_{GC}}$ is the Galactocentric distance to the source, which is 6.2 kpc for I15520 (T. Liu et al. 2020).

We estimate the outflow mass ($M_{\rm out}$), momentum ($P_{\rm out}$), energy ($E_{\rm out}$), and dynamical timescale ($t_{\rm dyn}$) using the following equations given in A. López-Sepulcre et al. (2009) and K. Wang et al. (2011):

$$M_{\rm out} = \sum_i M_{\rm i} = d^2 \left[\frac{\rm H_2}{\rm CO}\right] \mu_{\rm H}\, m_{\rm H} A \sum_i N_{\rm i}, \tag{5}$$

$$P_{\rm out} = \sum_i M_{\rm i} v_{\rm i}, \tag{6}$$

$$E_{\rm out} = \frac{1}{2} \sum_i M_{\rm i} v_{\rm i}^2, \tag{7}$$

$$t_{\rm dyn} = \frac{L_{\rm lobe}}{v_{\rm lobe}}, \tag{8}$$

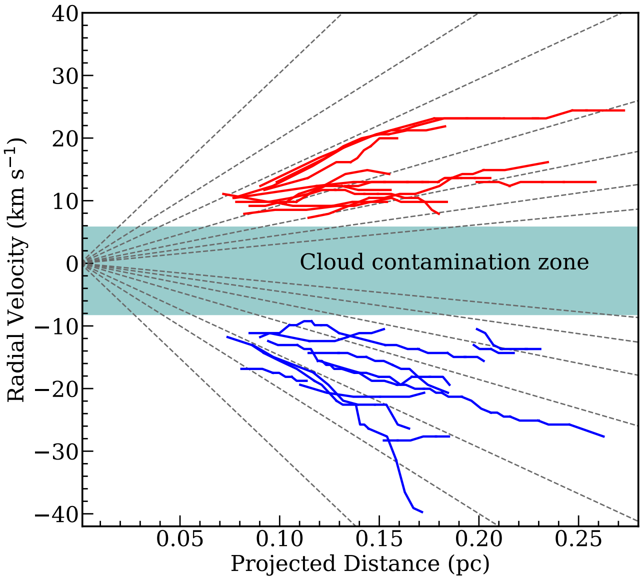

Figure 4. The position–velocity (P–V) diagram of the CO outflow fingers associated with I15520. The blue and red lines represent the P–V of the blueshifted and redshifted fingers, respectively. The radial velocities are given with respect to the cloud velocity. The projected distances are the distances measured from the explosive center. The gray lines represent a linear relationship between the radial velocity and the projected distances.

where $M_{\rm i}$ and $v_{\rm i}$ are the mass and velocity of each channel within the velocity range of the outflow, [CO/H$_2$] is the relative abundance of CO in comparison to H$_2$, d is the distance to the source, $\mu_{\rm H}$ is the mean molecular weight (adopted as 2.8), $m_{\rm H}$ is the mass of of the hydrogen atom, A is the angular sky area subtended by a single pixel, $N_{\rm i}$ is the column density for each velocity channel, $L_{\rm lobe}$ is the extent of the outflow lobe from the explosion center, and $v_{\rm lobe}$ is the terminal velocity of the outflow lobe. The value of [CO/H$_2$] is adopted as 10^{-4} (G. A. Blake et al. 1987). The observed outflow velocity is the line-of-sight component of the actual velocity, and the length of the outflow lobe is the plane of sky projection of the actual length. Therefore, for a better estimate of the outflow momentum and energy, a correction for the inclination angle needs to be applied. In this study, we assumed a mean inclination angle, θ, of $57\overset{\circ}{.}3$ (see M. M. Dunham et al. 2014 for detailed discussion) of the outflow fingers with respect to the line-of-sight direction and corrected the values of the outflow momentum ($P_{\rm out}$) and energy ($E_{\rm out}$) by multiplying them with $1/\cos\theta$ and $1/\cos^2\theta$, respectively. We estimate the mass, momentum, and energy of the explosive outflow by integrating the emissions of each channel over the velocity range of the explosive outflow. We included emissions $\geqslant 5\sigma$ in each channel for the estimation of outflow parameters, where σ is calculated from emission-free

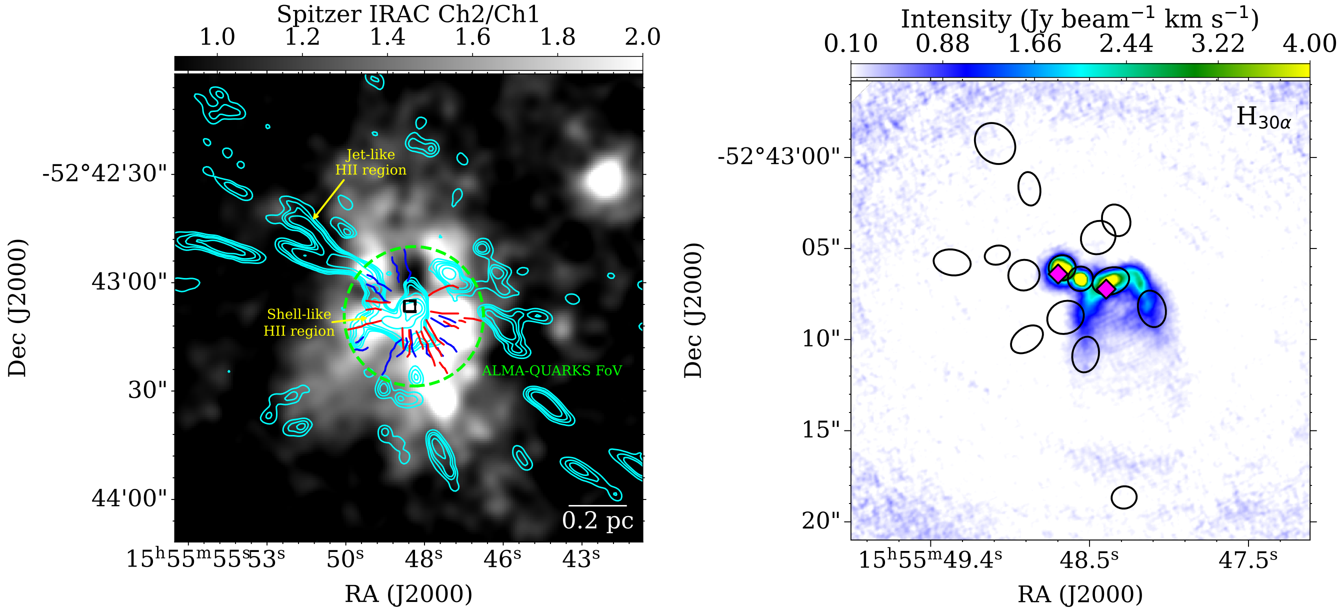

Figure 5. (Left) Spitzer ratio map Ch2 (4.5 μm)/Ch1 (3.6 μm) of I15520. The cyan contours represent the CORNISH 5.5 GHz radio continuum emission at the levels of [10, 20, 30, 50, 100]$\times\sigma$, where $\sigma = 0.2$ mJy beam^{-1}. The blue and red lines represent the blue- and redshifted outflow fingers, respectively. The center of the explosion is marked with a black rectangle. The green dashed circle represents the ALMA-QUARKS field of view. A scale bar is shown in the bottom-right corner. (Right) $H_{30\alpha}$ emission from the center of the protocluster I15520. The 1.3 mm continuum cores are marked as black ellipses. The magenta diamonds represent the two radio continuum peaks identified in the observations of G. Garay et al. (2006) using the ATCA.

channels. We calculate the total mass, momentum, and energy of the outflow as 23.8 $M_\odot$, 3129.8 $M_\odot$ km s^{-1}, and 4.1 × 10^{48} erg, respectively.

We estimate the dynamical timescale of the explosive event by assuming that outflow fingers are isotropic and have the same v_{3D}, and the difference in the observed extent and radial velocity is because of the different inclination angle of the outflow fingers. Therefore, the most likely estimate of the true extent of the explosive outflow would come from the longest projected outflow finger. Similarly, the most likely estimate of the true v_{3D} would come from the fastest (in the radial velocity) projected outflow finger. We find the extent of the explosive outflow to be 0.26 pc and the value of v_{3D} to be 38.5 km s^{-1}. The estimated dynamical age of the explosive outflow is 6550 yr.

Note that the estimated outflow parameters involve several observational biases, including the missing flux from interferometric observations, the distance uncertainty, the assumption of a constant outflow temperature, and a constant H_2-to-CO abundance ratio. Overall, these factors may result in the underestimation or overestimation of the outflow parameters by a factor of 2 to 3.

3.4. Radio Emission and Near-infrared Shocked Gas Associated with the Explosive Outflow

We use the Spitzer-IRAC ratio map Ch2(4.5 μm)/Ch1(3.6 μm) to identify the large-scale shock extent of the explosive source. The IRAC Ch2/Ch1 ratio map is capable of tracing shocked regions, as the Ch2 of the IRAC band includes shock-excited H_2 emission at 4.69 μm and Brα emissions at 4.05 μm, while Ch1 contains polycyclic aromatic hydrocarbon (PAH) features at 3.3 μm (M. S. Povich et al. 2007). In a detailed analysis of the Spitzer-IRAC bands toward six Herbig–Haro objects, M. Takami et al. (2010) reported that a flux ratio (Ch2/Ch1) $\geqslant$1.5 is dominated by shocked emissions, while a flux ratio $\ll$1.5 is indicative of stellar emissions. The left panel of Figure 5 represents the IRAC Ch2/Ch1 ratio map for I15520. The bright extended emission in the ratio map represents the shocked emissions in the region. The cyan contours in Figure 5 represent the 5.5 GHz radio continuum emissions associated with the explosive outflow. Two distinct morphologies of the radio continuum emissions can be visible. One is toward the explosive center where the radio emission traces a shell of H II region. In the outer regions, away from the center of explosion, the radio emission traces multiple extended jet-like structures. Although the morphology of these extended emissions suggests the possibility of candidate ionized jets, further high-resolution and high-sensitivity radio observations are required to confirm the nature of these structures.

In the right panel of Figure 5, we present the $H_{30\alpha}$ emission from the QUARKS survey. The $H_{30\alpha}$ emission traces two hypercompact H II regions and one cometary H II region, concentrated mostly toward the three massive cores located in the center of the cluster. G. Garay et al. (2006) previously reported the presence of two radio peaks at the center of explosion from the observations at 1.4, 2.5, 4.8, and 8.6 GHz using the Australia Telescope Compact Array (ATCA). In the right panel of Figure 5, we marked the two radio peaks from G. Garay et al. (2006) with magenta diamonds. The peaks of the radio emission coincide with two of the three H II regions detected in $H_{30\alpha}$ emission.

4. Discussion

4.1. Evidence of an Explosive Event

Our analysis reveals 28 narrow, high-velocity outflow fingers, following the Hubble–Lemaître velocity law, and possibly originating from a single event that occurred at the center of the protocluster. The outflow fingers are distributed

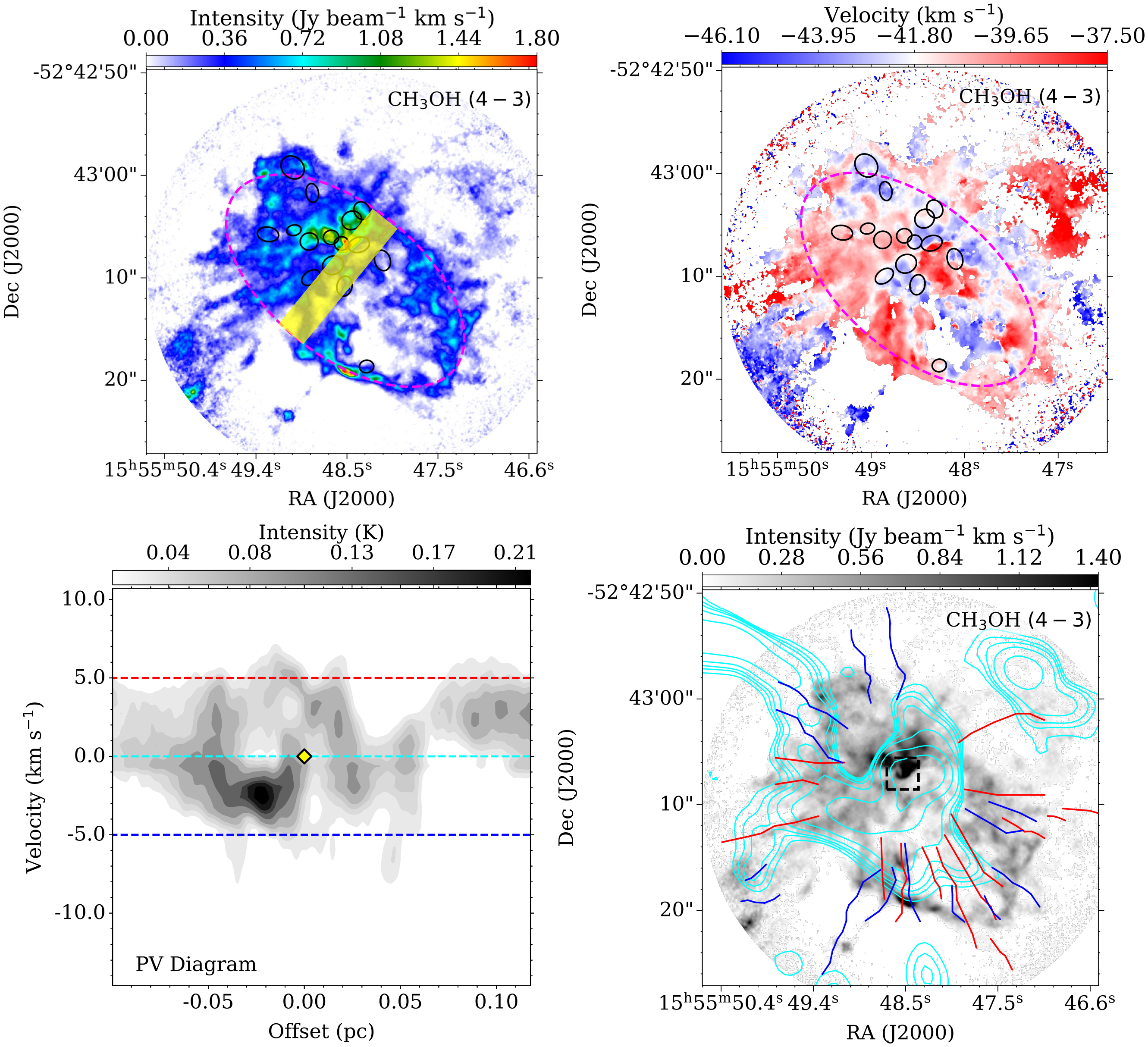

Figure 6. (Top) The ALMA CH$_3$OH (4−3) moment 0 (left) and moment 1 (right) map of the I15520 protocluster. The 1.3 mm continuum cores are shown as black ellipses. The magenta ellipse represents the tentative extent of the expanding CH$_3$OH shell. The yellow rectangle shows the path along which the P–V diagram is generated. (Bottom left) The P–V diagram along the length of the yellow rectangle in the CH$_3$OH moment 0 map generated from the northwest to southeast direction. The blue and red dashed lines represent the velocity extent of the blue- and redshifted expanding cloud with reference to the $V_{\rm LSR}$, respectively. The cyan dashed line represents the central velocity of the cloud. The center of the expanding shell is marked with a yellow diamond. (Bottom right) CH$_3$OH (4−3) moment 0, overlaid with the 5.5 GHz radio continuum contours (in cyan; the contours levels are the same as in Figure 5) and blue- and redshifted outflow fingers (in blue and red colored lines). The black dashed rectangle represents the center of the explosion.

quasi-isotropically with spatially overlapped blue- and redshifted fingers, and they do not have any bipolar counterparts. The outflow fingers point back to a common center, which approximately coincides with the center of the protocluster, where most of the massive cores are located. Regarding the kinematics, some of the blueshifted and redshifted fingers are spatially overlapped in projection, one of the key characteristics of explosive outflows. In addition, most outflow fingers show a velocity gradient with increasing velocity far from the center of the protocluster, which is also a distinctive signature of explosive outflows (e.g., E. Guzmán Ccolque et al. 2024; N. Issac et al. 2025). As in these other cases, shorter ejections show larger velocities and vice versa, supporting the tridimensional isotropic configuration of the outflow.

The estimated kinetic energy of the outflow is at least 4.1 × 10^{48} erg. Considering a large portion of initial kinetic energy may have been radiated away by the shocks, it suggests that the outflow associated with I15520 is a highly energetic explosive outflow. Its energy is at least 1 or 2 orders of magnitude higher than the typical energies of bipolar outflows associated with massive protostars (L. A. Zapata et al. 2017 and references therein). Finally, the mass and momentum of the outflow in I15520 are also similar to those found in other explosive outflows. Note that the angular resolution of the data

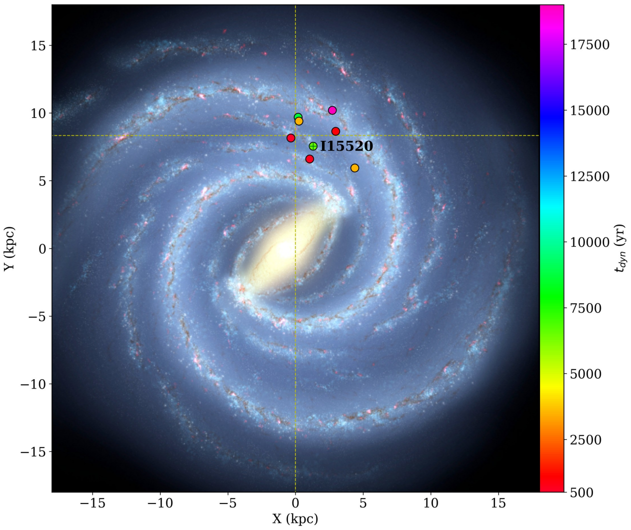

Figure 7. Projected spatial distribution of the confirmed explosive outflows in the Milky Way (artist's concept; R. Hurt: NASA/JPLCaltech/Spitzer Science Center). The positions of the explosive outflows are represented by colored dots. I15520 source is marked with a crossed dot. The color of the dots represents the dynamical age of the explosive outflows. The location of the Sun is marked by the crossing of the two dashed lines.

does not allow us to determine whether some of the continuum sources are receding from the common center, as seen in Orion Becklin-Neugebauer (BN)/Kleinman-Low (KL) outflow. Furthermore, due to the limitations in resolution and sensitivity, we cannot rule out the presence of a few individual bipolar outflows in the region, which are expected in an active star-forming region, like I15520, containing multiple HMCs. However, the overall kinematics and morphological evidence suggest the explosive nature of the outflow.

4.2. Expansion of CH_3OH Shell at the Center of Explosion

In dense star-forming regions, CH_3OH is known to trace shocked gas, mostly close to the systematic velocity of the cloud (J. Holdship et al. 2017; T. A. James et al. 2020; M. De Simone et al. 2024). Therefore, we utilize CH_3OH $J = 4(2, 2) -3(1, 2)$ (hereafter CH_3OH) emission to investigate its correlation with the explosive event and the shell-like H II region. In the top-left panel of Figure 6, the CH_3OH moment 0 map traces a shell-like structure around the explosive center, while the CH_3OH moment 1 map (in the top-right panel of Figure 6) shows a slightly blueshifted (toward northwest directions) and redshifted (toward southeast direction) velocity of the CH_3OH shell. A tentative extent of the expanding shell is drawn visually in the top panels of Figure 6. We further investigate the expanding CH_3OH shell by generating a P–V diagram along a rectangular strip across the shell. Figure 6 (bottom left) represents the P–V diagram across the expanding shell. The P–V diagram indicates that the CH_3OH shell is slowly expanding outward at velocities $\sim\pm 5$ km s^{-1} from the V_{LSR}. However, the center of expansion does not exactly coincide with the center of explosion.

We further investigate the spatial correlation of the CH_3OH shell with the 5.5 GHz radio continuum emission and also with the distribution of the outflow fingers. In the bottom-right panel of Figure 6, the CH_3OH moment 0 map is overlaid with contours (cyan) of 5.5 GHz radio continuum emission and blue- and redshifted outflows in blue and red colored lines, respectively. We find the distribution of the CH_3OH shell correlates well with both the shell of the H II region and also the distribution of the outflow fingers. Therefore, this suggests that the CH_3OH shell could have arisen due to compression of the ambient medium driven either by the shell of the H II region, by the explosive outflow, or by the combined effect of both mechanisms.

4.3. Rate of Explosive Events in the Milky Way

Until now, a total of seven explosive outflows have been reported in the the Milky Way (Orion BN/KL, DR21, G5.89 −0.39, IRAS 16076−5134, Sh2-106, IRAS 12326−6245, and G34.26+0.15). In this study, we have reported a new explosive outflow in I15520. In Figure 7, we present the spatial distribution of the confirmed explosive outflows in the the Milky Way, including our recent addition to the list, I15520. Based on the seven explosive sources identified earlier, N. Issac et al. (2025) estimated the rate of explosive events in the Galaxy to be one every 160 yr. However, the rate was earlier estimated by L. A. Zapata et al. (2023) by considering the first six explosive outflows in the Galaxy as one every 90 yr. With the inclusion of the newly detected I15520 explosive outflow, we reestimate the rate of explosive events following the same method described in E. Guzmán Ccolque et al. (2022) and L. A. Zapata et al. (2023). We assume that the explosive outflows are evenly distributed in time over a time span of 19,000 yr covering the time period of all eight explosive outflows (after taking into account their different distances to the Earth) and are distributed within a circle of diameter 5.6 kpc (the separation between the farthest known explosive outflows, IRAS 16076−5134 and DR21). We also assume that the Galaxy is a thin disk with a radius of 15 kpc and estimate the rate of explosive events, which is one event every 83 yr. Note that the method employed here is simplified and relies on several assumptions, such as the size of the Galaxy, constant star formation rate with galactocentric distance, and a rough estimate of the dynamical timescale of the outflow. The estimate will be more refined with more detections of the explosive outflows in the Galaxy. The estimated rate of explosive outflows is very similar to the massive star formation rate (one star every 50 yr; L. A. Zapata et al. 2023) and the rate of supernova formation (one every 50 yr; R. Diehl et al. 2006; L. A. Zapata et al. 2023). Therefore, it is possible that massive stars may undergo such explosive phases during their formation, and a more comprehensive study would be beneficial to deepen our understanding of massive star formation.

4.4. Possible Driving Mechanism of Explosive Events

The driving mechanisms for explosive outflows have been investigated in multiple studies. Among them, the most compelling and observationally supported explanations are the rearrangement of nonhierarchical systems and their dynamical interactions (J. Bally et al. 2011). A simulation study by P. R. Rivera-Ortiz et al. (2021) involving the close encounter of a massive star with a cluster of particles also produced outflow fingers that resemble the explosive outflow observed in Orion BN/KL. In I15520, we find that the continuum cores located within the protocluster are mass segregated, with most of the massive cores located close to the center of the protocluster, and the less massive cores are located in the outer region of the protocluster. The central massive cores (C1, C2, and C3) are separated by a sky-projected distance of ∼4000 au, while their sizes (∼3500 −5400 au) are also comparable to this distance. Mass segregation in I15520 was also previously reported in F. Xu et al. (2023) using ALMA band 7 observations. It is possible that the protocluster had undergone a rearrangement of masses, and the dynamical interaction among the central massive cores may result in the formation of explosive outflows. Previous observations of G. Garay et al. (2006) identified an extended H II region at the center of the protocluster. The authors also determined the spectral types of the ionizing sources and suggested the presence of two massive stars of spectral types O9.5 and B0. Therefore, an encounter of these massive stars with the massive protocluster could also be a possible mechanism for the formation of the explosive event. But the data used in this analysis preclude us from verifying the exact driving mechanism. High-resolution, more sensitive observations are needed to investigate the center of the explosion at scales of ∼100–1000 au to confirm the driving mechanism of the explosive event.

5. Summary

In this study, we have presented the high-resolution ALMA band 6 observations of the massive star-forming region, I15520. We found 28 well-collimated, molecular outflow fingers, most of which follow a Hubble–Lemaître velocity law. We estimated the total mass, momentum, and energy of the outflow fingers, which are at least 23.8 $M_{\odot}$, 3129.8 $M_{\odot}$ km s^{-1}, and 4.1 × 10^{48} erg, respectively. We found that all the outflow fingers emerged from a common center, which almost coincides with the center of the massive protocluster. The common center also coincides with the position of the UCH II region. These characteristics of the I15520 outflow fingers resemble all the characteristics of explosive outflows previously reported in the literature. We derived the dynamical age of this explosive event as ∼6550 yr. We reestimated the rate of explosive outflows in the Galaxy, which is one event every ∼83 yr. We found that the compact cores within the protocluster are mass segregated, with most of the massive cores being at the center. We speculate that the dynamical interactions among these massive cores might be the origin of this explosive event.

Acknowledgments

We thank the anonymous referee for valuable comments and suggestions, which greatly improved the quality of the manuscript. A.H. and T.B. thank the support of the S. N. Bose National Centre for Basic Sciences under the Department of Science and Technology, Govt. of India. A.H. also thanks the CSIR-HRDG, Govt. of India, for funding the fellowship. This work was performed in part at the Jet Propulsion Laboratory, which is operated by the California Institute of Technology under contract with the National Aeronautics and Space Administration (80NM0018D0004). S.R.D. acknowledges support from the Fondecyt Postdoctoral fellowship (project code 3220162) and ANID BASAL project FB210003. N.K.B. acknowledges the support of the China Postdoctoral Science Foundation through grant No. 2025M773187. L.B. and G.G. gratefully acknowledge support by the ANID BASAL project FB210003.

This paper utilizes the following ALMA dataset: ADS/JAO.ALMA#2021.1.00095.S. ALMA is a partnership of ESO (representing its member states), NSF (USA), and NINS (Japan), together with NRC (Canada), MOST and ASIAA (Taiwan), and KASI (Republic of Korea), in cooperation with the Republic of Chile. The Joint ALMA Observatory is operated by ESO, AUI/NRAO, and NAOJ.

Facility: ALMA.

Software: astropy (Astropy Collaboration et al. 2013), spectral-cube (A. Ginsburg et al. 2019), APLpy (T. Robitaille & E. Bressert 2012), SAOds9 (Smithsonian Astrophysical Observatory 2000).

Appendix A
CO Channel Maps of the Explosive Outflow in the I15520 Region

In this appendix, we present the CO channel maps of the blue- and redshifted components of the explosive outflow in the I15520 region in Figures A1 and A2. A detailed description of Figures A1 and A2 is in Section 3.2.

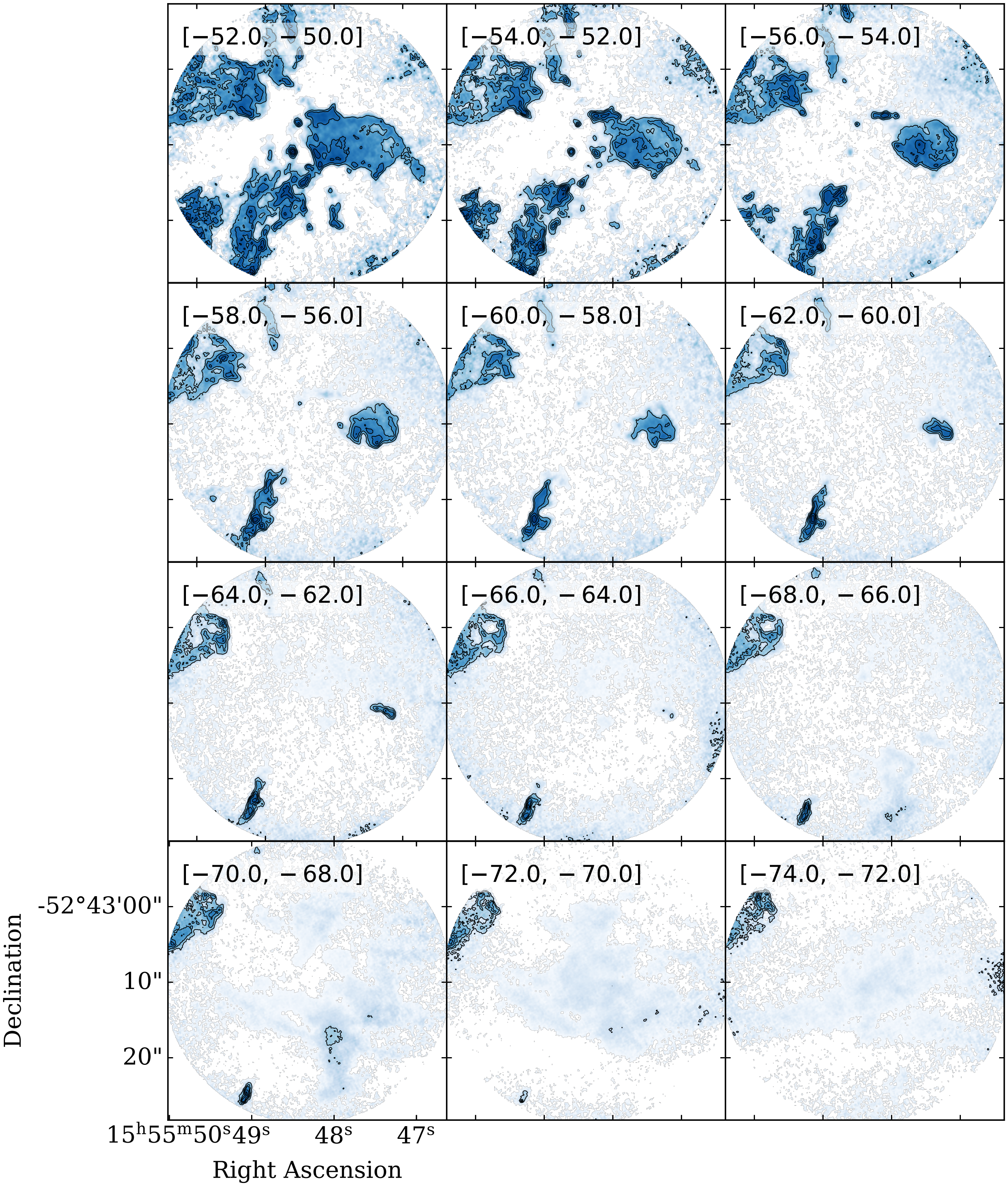

Figure A1. The ALMA CO channel maps of the blueshifted outflow wings in the I15520 region. Each panel represents the integrated intensity map within the velocity range as mentioned (in km s^{-1}) in each channel.

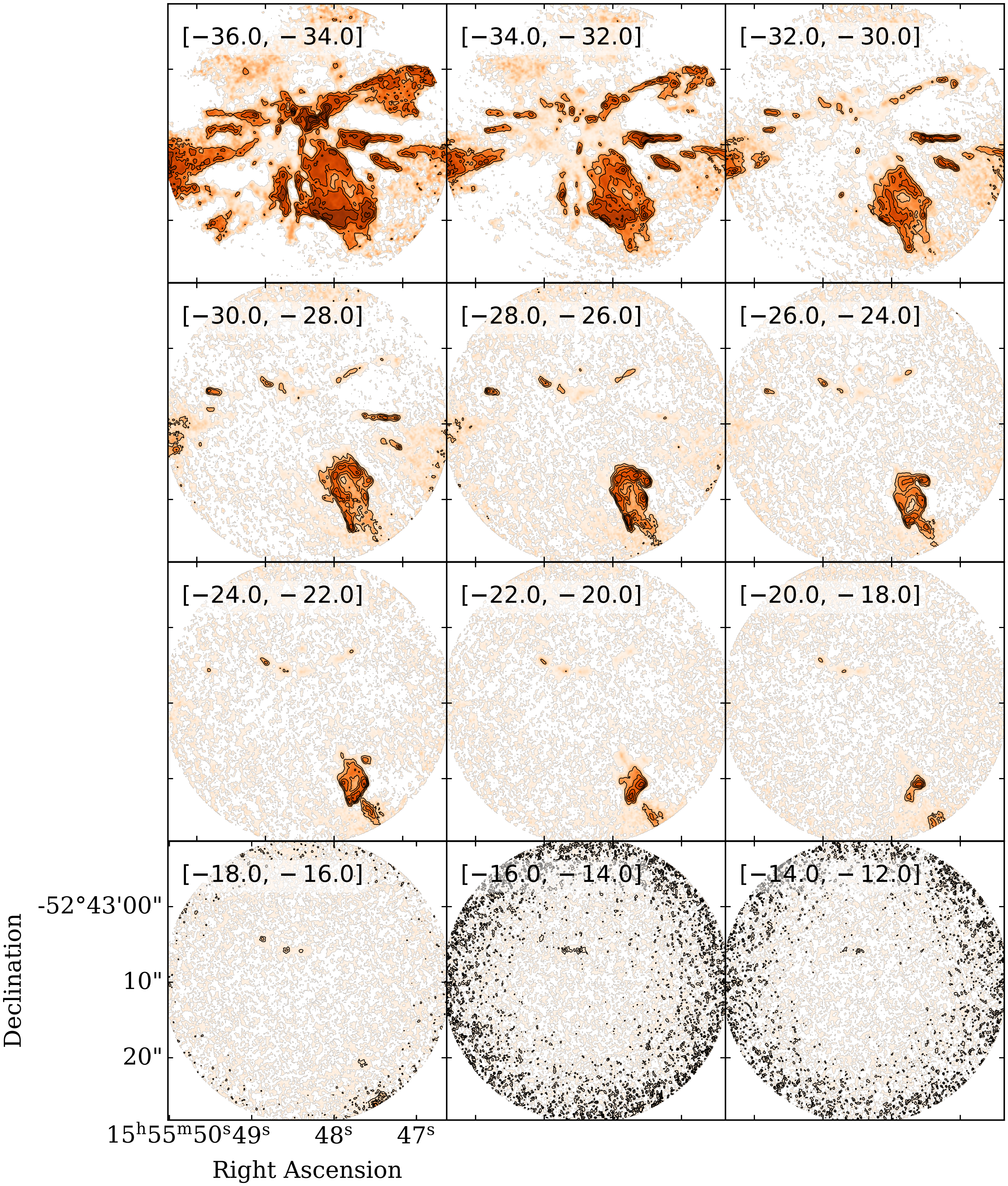

Figure A2. The ALMA CO channel maps of the redshifted outflow wings in I15520 region. Each panel represents the integrated intensity map within the velocity range as mentioned (in km s^{-1}) in each channel.

Appendix B

Distances of the Compact Cores from the Explosive Center

In this appendix, we present the sky-projected distances of the compact cores from the explosive center. Figure B1 shows the distribution of core masses with the sky-projected distance from the center of explosion.

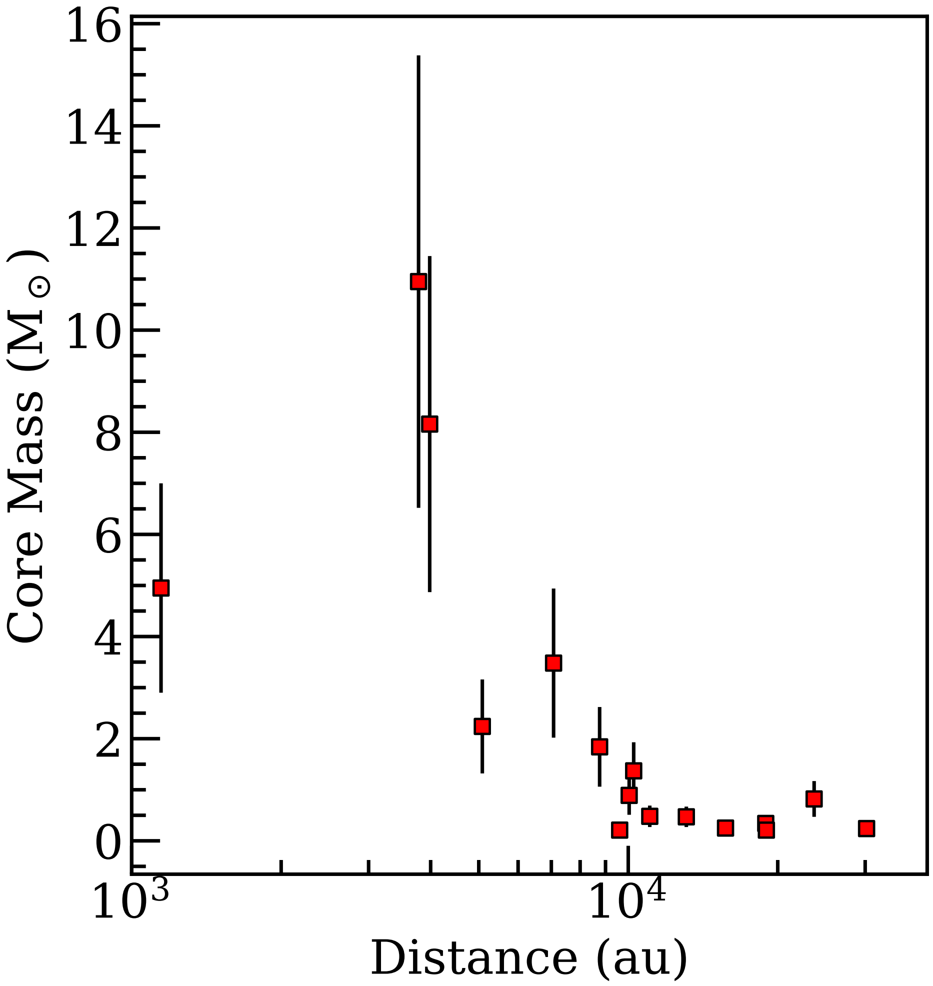

Figure B1. Scatterplot of core mass versus projected distance from the explosive center for the compact cores in I15520. The uncertainty in the core mass is shown with black error bars.

Appendix C
Additional Moment Maps of Outflow Tracers

In this appendix, we present the moment 0 and 1 maps of SiO (5−4), SO (6−5), and ^{13}CO (2−1) molecular lines from the QUARKS survey. In Figure C1, left and right panels, we present the intensity and velocity distribution of the molecular lines, respectively, tracing the morphology and kinematics of the outflow fingers.

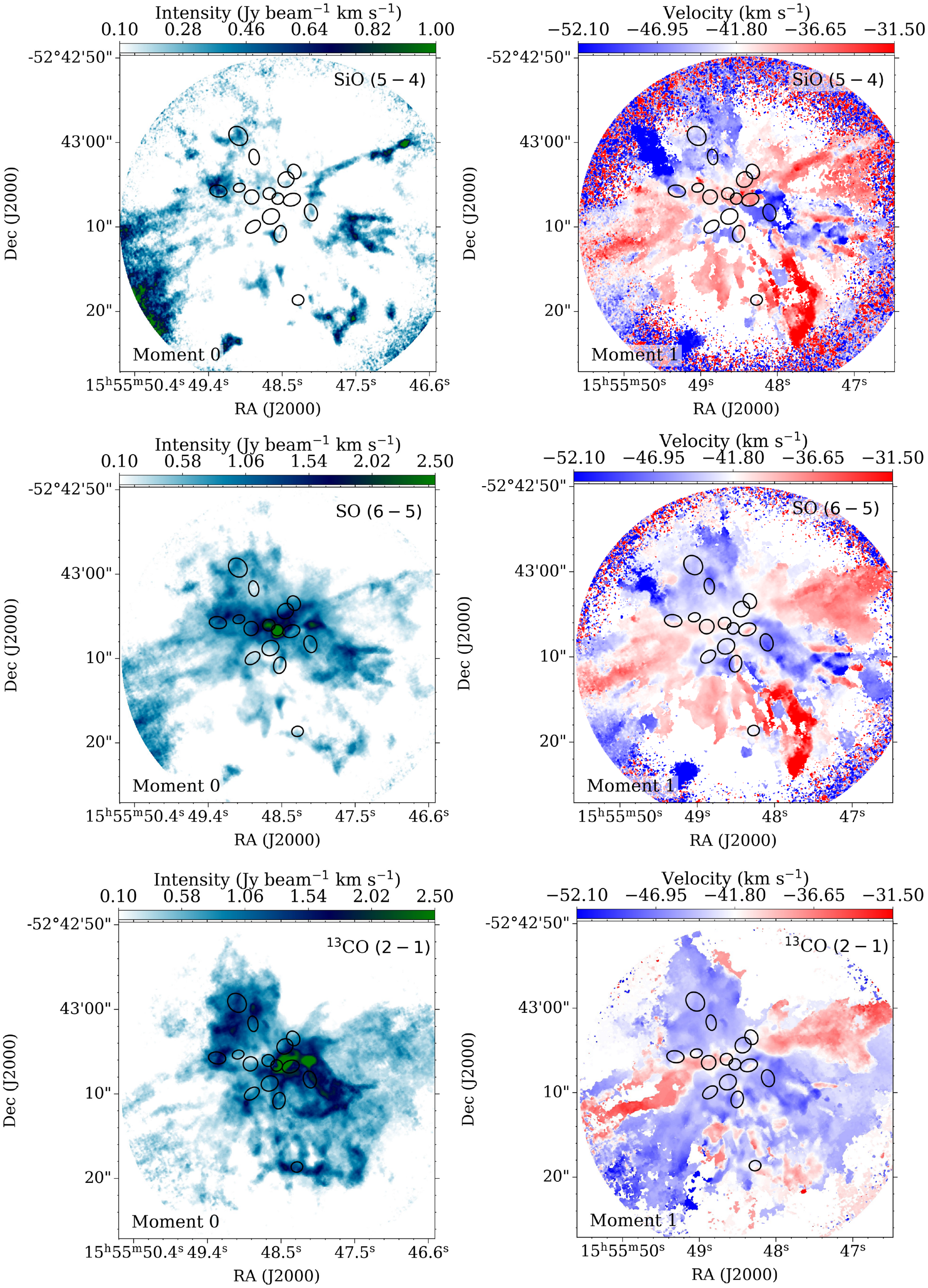

Figure C1. Moment 0 (left) and moment 1 (right) maps of outflow tracers covered in the QUARKS survey. The name of the molecular line is quoted in the top-right corner of each plot. The 1.3 mm continuum cores are shown as black ellipses.

ORCID iDs

Ariful Hoque https://orcid.org/0009-0003-6633-525X
Tapas Baug https://orcid.org/0000-0003-0295-6586
Estrella Guzman https://orcid.org/0000-0003-2630-3774
Manuel Fernandez Lopez https://orcid.org/0000-0001-5811-0454
Tie Liu https://orcid.org/0000-0002-5286-2564
Guido Garay https://orcid.org/0000-0003-1649-7958
Paul F. Goldsmith https://orcid.org/0000-0002-6622-8396
Fengwei Xu https://orcid.org/0000-0001-5950-1932
Xindi Tang https://orcid.org/0000-0002-4154-4309
Patricio Sanhueza https://orcid.org/0000-0002-7125-7685
Lokesh K. Dewangan https://orcid.org/0000-0001-6725-0483
Shivani Gupta https://orcid.org/0000-0002-8614-0025
Sami Dib https://orcid.org/0000-0002-8697-9808
Luis A. Zapata https://orcid.org/0000-0003-2343-7937
Jihye Hwang https://orcid.org/0000-0001-7866-2686
N. K. Bhadari https://orcid.org/0000-0001-8812-8460
John Bally https://orcid.org/0000-0001-8135-6612
Swagat Ranjan Das https://orcid.org/0000-0002-3658-0516
Aiyuan Yang https://orcid.org/0000-0003-4546-2623
Prasanta Gorai https://orcid.org/0000-0003-1602-6849
Arup Kumar Maity https://orcid.org/0000-0002-7367-9355
James O. Chibueze https://orcid.org/0000-0002-9875-7436
Pablo García https://orcid.org/0000-0002-8586-6721
Leonardo Bronfman https://orcid.org/0000-0002-9574-8454
Xunchuan Liu https://orcid.org/0000-0001-8315-4248
L. Viktor Tóth https://orcid.org/0000-0002-5310-4212
Shehu Muhammad Usman https://orcid.org/0009-0002-5015-9979
Kee-Tae Kim https://orcid.org/0000-0003-2412-7092

References

Arce, H. G., Borkin, M. A., Goodman, A. A., Pineda, J. E., & Halle, M. W. 2010, ApJ, 715, 1170
Arce, H. G., & Goodman, A. A. 2001, ApJ, 551, L171
Astropy Collaboration, Robitaille, T. P., Tollerud, E. J., et al. 2013, A&A, 558, A33
Bachiller, R. 1996, ARA&A, 34, 111
Bally, J., Chia, Z., Ginsburg, A., et al. 2022, ApJ, 924, 50
Bally, J., Cunningham, N. J., Moeckel, N., et al. 2011, ApJ, 727, 113
Baug, T., Wang, K., Liu, T., et al. 2020, ApJ, 890, 44
Benjamin, R. A., Churchwell, E., Babler, B. L., et al. 2003, PASP, 115, 953
Blake, G. A., Sutton, E. C., Masson, C. R., & Phillips, T. G. 1987, ApJ, 315, 621
De Simone, M., Podio, L., Chahine, L., et al. 2024, A&A, 686, L13
Diehl, R., Halloin, H., Kretschmer, K., et al. 2006, Natur, 439, 45
Dunham, M. M., Arce, H. G., Mardones, D., et al. 2014, ApJ, 783, 29
Ellingsen, S. P., Shabala, S. S., & Kurtz, S. E. 2005, MNRAS, 357, 1003
Garay, G., Brooks, K. J., Mardones, D., & Norris, R. P. 2006, ApJ, 651, 914
Garden, R. P., Hayashi, M., Gatley, I., Hasegawa, T., & Kaifu, N. 1991, ApJ, 374, 540
Ginsburg, A., Koch, E., Robitaille, T., et al. 2019, radio-astro-tools/spectral-cube: v0.4.4, Zenodo, doi:10.5281/zenodo.2573901
Goldsmith, P. F., & Langer, W. D. 1999, ApJ, 517, 209
Guerra-Varas, N., Merello, M., Bronfman, L., et al. 2023, A&A, 677, A148
Guzmán Ccolque, E., Fernández-López, M., Zapata, L. A., & Baug, T. 2022, ApJ, 937, 51
Guzmán Ccolque, E., Fernández López, M., Zapata, L. A., Bally, J., & Rivera-Ortiz, P. R. 2024, A&A, 689, A339
Hatchell, J., Fuller, G. A., & Ladd, E. F. 1999, A&A, 344, 687
Holdship, J., Viti, S., Jiménez-Serra, I., Makrymallis, A., & Priestley, F. 2017, AJ, 154, 38
Hoque, A., Baug, T., Dewangan, L. K., et al. 2025, ApJ, 987, 197
Irabor, T., Hoare, M. G., Burton, M., et al. 2023, MNRAS, 520, 1073
Issac, N., Lu, X., Liu, T., et al. 2025, AJ, 169, 324
Izumi, N., Sanhueza, P., Koch, P. M., et al. 2024, ApJ, 963, 163
James, T. A., Viti, S., Holdship, J., & Jiménez-Serra, I. 2020, A&A, 634, A17
Li, Z.-Y., & Shu, F. H. 1996, ApJ, 472, 211
Liu, T., Evans, N. J., Kim, K., et al. 2020, MNRAS, 496, 2790
Liu, X., Liu, T., Zhu, L., et al. 2024, RAA, 24, 025009
López-Sepulcre, A., Codella, C., Cesaroni, R., Marcelino, N., & Walmsley, C. M. 2009, A&A, 499, 811
Mangum, J. G., & Shirley, Y. L. 2015, PASP, 127, 266
Maud, L. T., Moore, T. J. T., Lumsden, S. L., et al. 2015, MNRAS, 453, 645
Men'shchikov, A. 2021, A&A, 649, A89
Möller, T., Endres, C., & Schilke, P. 2017, A&A, 598, A7
Müller, H. S. P., Thorwirth, S., Roth, D. A., & Winnewisser, G. 2001, A&A, 370, L49
Povich, M. S., Stone, J. M., Churchwell, E., et al. 2007, ApJ, 660, 346
Qiu, K., Zhang, Q., Wu, J., & Chen, H.-R. 2009, ApJ, 696, 66
Raga, A. C., Rivera-Ortiz, P. R., Cantó, J., Rodríguez-González, A., & Castellanos-Ramírez, A. 2021, MNRAS, 508, L74
Rivera-Ortiz, P. R., Rodríguez-González, A., Cantó, J., & Zapata, L. A. 2021, ApJ, 916, 56
Rivera-Ortiz, P. R., Rodríguez-González, A., Cantó, J., et al. 2025, ApJ, 986, 71
Robitaille, T., & Bressert, E. 2012, APLpy: Astronomical Plotting Library in Python, Astrophysics Source Code Library, ascl:1208.017
Sanhueza, P., Jackson, J. M., Foster, J. B., et al. 2012, ApJ, 756, 60
Shimajiri, Y., Takahashi, S., Takakuwa, S., Saito, M., & Kawabe, R. 2009, PASJ, 61, 1055
Shu, F. H., Ruden, S. P., Lada, C. J., & Lizano, S. 1991, ApJL, 370, L31
Smithsonian Astrophysical Observatory 2000, SAOImage DS9: A utility for displaying astronomical images in the X11 window environment, Astrophysics Source Code Library, ascl:0003.002
Takami, M., Karr, J. L., Koh, H., Chen, H.-H., & Lee, H.-T. 2010, ApJ, 720, 155
Tang, X. D., Henkel, C., Menten, K. M., et al. 2018, A&A, 609, A16
Towner, A. P. M., Ginsburg, A., Dell'Ova, P., et al. 2024, ApJ, 960, 48
Urquhart, J. S., König, C., Giannetti, A., et al. 2017, MNRAS, 473, 1059
Wang, K., Zhang, Q., Wu, Y., & Zhang, H. 2011, ApJ, 735, 64
Wilson, T. L., & Rood, R. T. 1994, ARA&A, 32, 191
Xu, F., Wang, K., Liu, T., et al. 2023, ApJS, 270, 9
Yang, D., Liu, H.-L., Liu, T., et al. 2025, ApJS, 280, 33
Zapata, L. A., Fernández-López, M., Leurini, S., et al. 2023, ApJL, 956, L35
Zapata, L. A., Ho, P. T. P., Guzmán Ccolque, E., et al. 2019, MNRAS, 486, L15
Zapata, L. A., Schmid-Burgk, J., Ho, P. T. P., Rodríguez, L. F., & Menten, K. M. 2009, ApJ, 704, L45
Zapata, L. A., Schmid-Burgk, J., Pérez-Goytia, N., et al. 2013, ApJL, 765, L29
Zapata, L. A., Schmid-Burgk, J., Rodríguez, L. F., Palau, A., & Loinard, L. 2017, ApJ, 836, 133